




# Microstructural and hardness evolution of additively manufactured Al–Si–Cu alloy processed by high-pressure torsion

Ahmed S. J. Al-Zubaydi<sup>1,2,\*</sup> , Nong Gao<sup>1</sup>, Shuncaï Wang<sup>1</sup>, and Philippa A. S. Reed<sup>1</sup>

<sup>1</sup>School of Engineering, Faculty of Engineering and Physical Sciences, University of Southampton, Southampton SO17 1BJ, UK

<sup>2</sup>School of Applied Sciences, University of Technology-Iraq, Baghdad, Iraq

Received: 10 January 2022

Accepted: 13 April 2022

Published online:  
6 May 2022

© The Author(s) 2022

## ABSTRACT

Nanostructured Al-9%Si-3%Cu alloy was achieved by direct metal laser sintering (DMLS) and then processed using high-pressure torsion (HPT) processing, which resulted in considerable grain refinement down to 60 nm associated with a substantial dislocation density up to  $6.2 \times 10^{14} \text{ m}^{-2}$  and a significant reduction in the porosity. Hardness measurements across the horizontal and vertical cross sections showed an improvement in the strength homogeneity for processed samples after 10 turns of HPT processing. These results indicate that a controllable ultrafine-grained microstructure can be achieved by employing additive manufacturing, followed by effective severe plastic deformation processing.

## Introduction

Additive manufactured alloys are emerging engineering materials with benefits of controllable microstructures and 3D customized shapes to fit challenges in the industrial needs [1, 2]. Additive manufacturing of aluminium light alloys has received considerable attention because of the capability to control the alloying contents precisely, thus achieving the required properties and performance, as well as their high strength-to-weight ratio. Several techniques have been used in fabrication of additive

manufactured aluminum alloys such as selective laser melting for Al–Si–Mg alloy [3, 4], Al–Si–Cu alloy [5], Al–Si alloy [6, 7], and direct metal laser sintering for Al–Si–Mg [8], Al–Cu–Mg/SiC composite [9]. In particular, the Al–Si–Cu alloys are employed in engine parts as engine blocks and pistons [10]. Alloying aluminum with silicon improves the casting fluidity, whereas adding copper and magnesium enhances solid solution and precipitation strengthening [11–13]. Considering the benefits of the additive manufactured alloy, some inevitable drawbacks come within their directly processed microstructures such as high porosity and powder

Handling Editor: Megumi Kawasaki.

Address correspondence to E-mail: asaz1f20@soton.ac.uk

clusters that can cause serious cracking in the manufactured parts [2, 14]. Recently, new approaches have been adopted to control such drawbacks and alter the properties of the additive manufactured alloys. High-pressure torsion (HPT) was employed as an efficient technique for severe plastic deformation (SPD) to process selective laser melted Al–Si–Mg [3], 316 stainless steel [15] and Co–Cr–Fe–Ni [16]. These studies have focused only on horizontal cross sections of the HPT samples, where the vertical cross sections of these samples have not been investigated. Therefore, the current work focuses on the microstructural homogeneity over both horizontal and vertical cross sections for direct metal laser melted Al-9%Si-3%Cu alloy processed using high-pressure torsion. The study includes the evolution of grain refinement of the aluminium matrix and eutectic silicon phase, and porosity content as measured by different approaches. The distribution of eutectic nano-sized particles and evolution of dislocation density have also been inspected to evaluate the resultant strength in the additive manufactured processed alloy. Evaluating the relationship between the achieved microstructure and subsequent properties in the additive manufactured aluminum alloys processed by HPT will improve the understanding and knowledge of this processing technique in the densification and strengthening of these alloys. As well, this alloy is widely used in the manufacture of engine blocks and parts, therefore, alteration of the microstructure of the additive manufactured alloy will result in improved properties toward better performance under operating conditions at ambient and high temperatures.

## Materials and methods

Table 1 shows the compositions of the Al-9%Si-3%Cu alloy manufactured by direct metal laser sintering (DMLS). The alloy was manufactured using a Concept Laser M2 machine under nitrogen atmosphere at room temperature using the following parameters: 200 W of laser power, 1000 mm/s of scan speed, 200  $\mu\text{m}$  of hatch spacing, and 40  $\mu\text{m}$  of layer thickness. The alloy was additively manufactured as a cylindrical rod of 150 mm in length and 11 mm in diameter. This alloy was built along the vertical direction relative to the manufacturing area as illustrated in Fig. 1. A wire discharge machine was

**Table 1** Chemical analysis (%wt) of the additive manufactured Al-9%Si-3%Cu alloy

	Al	Si	Cu	Fe	Mg
Al–Si–Cu	Bal	9.1	3.2	0.5	0.3

employed to reduce the diameter of the rod alloy to 9.8 mm and cut to disks of thickness 1 mm. The disks were thinned to thicknesses of 0.85 mm by 800 grit abrasive paper in order to be placed between the HPT anvils. Under a quasi-constrained condition, HPT processing was achieved [17, 18], using the following parameters: 6.0 GPa applied pressure, 1 rpm rotational speed and number of turns ( $N$ ) of 1/2, 1, 3, 5 and 10 turns at room temperature. The final average thickness of the HPT processed sample after 10 turns was  $\sim 0.7$  mm. The following investigations were carried out on as-received and processed samples: microstructural observations, X-ray diffraction analysis, porosity and microhardness measurements. The samples were mechanically ground and polished using abrasive papers of (800–4000) grit and 1  $\mu\text{m}$  diamond paste, respectively. These samples were etched using Keller's reagent for 10 s and then cleaned with ethanol and compressed air, respectively. Then, the microstructures were observed through the horizontal and vertical cross sections that are represented in Fig. 1 using optical microscopy (OM, OLYMPUS-BX51) [19]. Scanning electron microscopy (SEM, FEI Quanta 200) was conducted on the horizontal cross sections of the etched samples. Elemental mapping of the as-received alloy was obtained using the energy-dispersive spectroscopy (EDS) to determine the chemical composition with weight fractions. Transmission electron microscopy (TEM, JEOL JEM-3010) was conducted to observe the microstructure at the edge region of each disk. Samples of 3 mm in diameter and 100  $\mu\text{m}$  in thickness were taken from these areas and then subjected to electropolishing in 30% vol. of nitric acid in methanol at 20 V and 243 K using twin-jet electro-polishing facility (Struers). Patterns of the X-ray diffraction (XRD), size of crystallite domains and density of dislocations were attained from X-ray analysis of the as-received and processed samples using an XRD analyzer (Bruker, D2 Phaser) using a  $K\alpha$ -Cu with wavelength of 0.154 nm and a step size of  $0.02^\circ$  from  $2\theta$  range of  $30$ – $90^\circ$ . The recorded data were refined

using MAUD software using Rietveld refinement of the full peak X-ray profile based on aluminum peaks [19, 20]. The dislocation density ( $\rho$ ) was computed via XRD data through the following relationship [18]:  $\rho = 2\sqrt{3}\varepsilon/d_c b$ , where  $\varepsilon$  is the average microstrain,  $d_c$  is the average crystallite size; both values have been gained by MAUD software, and  $b$  is the vector of Burgers for the aluminum (0.286 nm [21]).

The area fraction of the eutectic silicon phase particles was calculated by employing the SEM micrographs and ImageJ analysis software. Area fraction of particles refers here to the particles total number times their average area divided by the field area on SEM micrograph [22]. Random locations on each SEM micrograph for each etched sample were selected as field areas, which transformed into black and white field areas using ImageJ software to calculate the area fraction of particles.

The porosity was measured through both Archimedes principle approaches and ImageJ analysis of OM micrographs [23, 24]. In the Archimedes method, an average of five readings for each mass measurement was recorded using a digital balance to four-digits accuracy [24, 25]. In ImageJ software analysis of OM micrographs, areas in OM micrographs of (3000 × 3000) mm<sup>2</sup> across the horizontal cross sections, and (1000 × 1000) mm<sup>2</sup> across the vertical cross sections were taken for the as-received and processed samples. This procedure was repeated over several OM micrographs for different cross sections to ensure more reliable measurement of porosity. The porosity was calculated according to the ASTM E562-01 [26] and average pore diameter was obtained using ImageJ software analysis in the pixelated OM micrographs. Vickers microhardness was recorded for the as-received and processed samples across both polished horizontal and vertical cross sections using a microhardness tester with 100 gf load for 15 s, and the recorded results were constructed as colour-coded maps using similar procedures as detailed in Ref. [19].

## Results

### Microstructural observations

The optical microstructures of the as-received material and that obtained after 10 HPT turns in the central region of the disks are shown, respectively, in

Fig. 2a–c. These micrographs were taken over the horizontal cross sections of the disks. The as-received sample in the horizontal disk plane clearly shows melt pools with average width of 150 μm and different lengths, showing the island scanning strategy perpendicular to the build direction of the rod. Both process-induced and gas-induced porosities were observed in the polished and etched as-received samples, as indicated, respectively, by solid and dashed circles (Fig. 2a, b). However, a different pool morphology was observed in the samples after HPT processing, where these pools have been sheared along with the direction of HPT strain as the number of turns increased up to 10 turns as indicated by curved dashes arrows in Fig. 2c. The microstructures over the vertical cross sections of the as-received (parallel to the build direction) and HPT-processed samples are shown in Fig. 2d–f. A fish-scale like morphology is shown in the as-received sample, whereas an elongated microstructure is exhibited in the HPT-processed sample, as indicated by the straight arrows. SEM observations of etched samples revealed two main phases, dark  $\alpha$ -Al matrix and white eutectic Si continuous network, as seen in Fig. 3a. Process-induced porosity embedded with a few nonmelted powder particles can also be seen in Fig. 3b. The morphology of the alloy was altered following HPT processing as seen in Fig. 4a–f, where the eutectic phase has undergone a gradual fragmentation at the peripheries of processed disks as the number of HPT turns increased as exhibited in Fig. 4a, b. In addition, this phase has been sheared clearly toward the torsional HPT strain as indicated by yellow solid arrows in Fig. 4c–f. Finally, this phase showed relatively homogeneous distribution of eutectic nano-sized particles at the peripheries of processed samples as indicated by the area fraction measurements and illustrated in Fig. 5.

TEM observations of the HPT-processed microstructures at the edges of disks showed extensive grain refinement at early stages of HPT processing as revealed in Fig. 6a–c, with grain size of 150 nm after 1/2 turn, down to 60 nm after processing up to 10 turns. XRD patterns for the as-received sample exhibited several peaks, identified as belonging to aluminum and silicon, confirming the EDS data establishing the compositional analysis of the current alloy, as indicated in Fig. 7a. Post-HPT processing, aluminum (111) and (200) peaks continued to appear, silicon (220) and (311) peaks

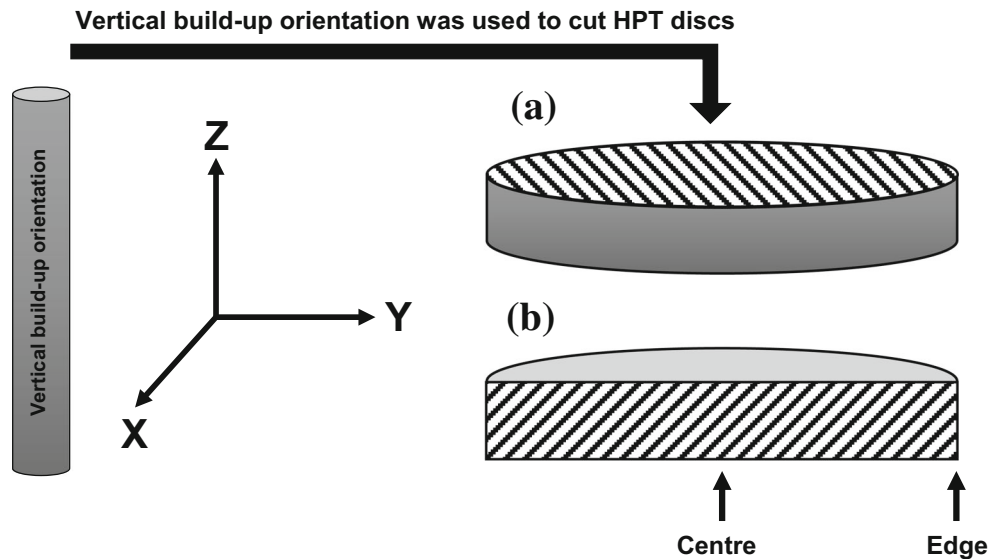


**Figure 1** Schematic illustrations of: (left) Vertical build-up orientation of the alloy rod during DLMS that adopted in the current investigation, and (right) Sample orientation of HPT disc that cut from the alloy rod through vertical build-up orientation

disappeared and a shift in peak locations was observed for the processed sample in comparison with the as-received sample as illustrated in Fig. 7b. The fitted XRD pattern of sample processed for 10 turns using the Rietveld refinement procedure, and the values of microstrain and lattice parameter in the as-received and processed samples are shown in Fig. 7c, d.

### Porosity measurements

A comparison of porosity between the as-received samples and after 10 HPT turns shows a significant reduction in the porosity fraction after HPT processing to about 73, 90 and 96%, respectively, based on measurements conducted by the Archimedes method, ImageJ analysis on (1) the horizontal and (2) vertical cross sections at the peripheries of the disks, as shown in Fig. 8. Considerable reduction in porosity fraction and pore diameter was noticed with increasing number of HPT turns in the horizontal cross sections at the peripheries of the disks, as illustrated in Fig. 9. Porosity fraction and average pore diameter are 0.3% and 7  $\mu\text{m}$  for the as-received sample and 0.03% and 0.5  $\mu\text{m}$  in the edge region of the horizontal cross section of the sample processed for 10 turns.

showing: a horizontal and b vertical cross sections that used for microstructural observations and microhardness measurements [19].

### Hardness measurements

The microhardness distribution recorded on the horizontal and vertical cross sections of the as-received and processed samples are illustrated in Figs. 10 and 11. The as-received sample showed a Vickers microhardness about 120 Hv. After HPT processing, a gradual increasing evolution in the hardness was recorded throughout these cross sections. The hardness evolution started at a faster rate in the peripheral areas of the deformed disks than in the central regions. A fairly saturated homogeneity in hardness was obtained for samples processed up to 10 turns across the horizontal and vertical cross sections, where the hardness value was about 240 Hv, twice that for the as-received sample. In general, the maximum values of achievable hardness after HPT processing on the horizontal cross sections of HPT disks were 180, 200, 206, 220 and 240 Hv in the samples processed for 1/2, 1, 3, 5 and 10 turns, respectively. A similar increase was obtained in the maximum achievable hardness across the vertical cross sections of HPT disks of 170, 190, 200, 210 and 230 Hv in the samples processed for 1/2, 1, 3, 5 and 10 turns, respectively. The trend of hardness evolution was correlated with the development in crystallite size obtained from XRD analysis and TEM of the grain size as shown in Fig. 12.

Vickers microhardness has shown a significant improvement with increasing number of HPT turns that is accompanied with a considerable decrease in the size of crystallites from 320 nm in the as-received sample to 30 nm in the sample deformed for 10 HPT turns. The same trend has been observed in TEM analysis where the minimum grain size appeared to be 60 nm. The hardness was also correlated with the dislocation density as illustrated in Fig. 13. The as-received sample gave a density of dislocation of  $1.1 \times 10^{14} \text{ m}^{-2}$ , whereas this value has increased to  $6.2 \times 10^{14} \text{ m}^{-2}$  in the sample processed for 10 HPT turns. Empirical Hall–Petch and Taylor relationships [27, 28]:  $Hv = H_0 + kd^{-1/2}$  and  $Hv = H_0 + \alpha M G b \rho^{1/2}$ , respectively, were calculated for the current processed alloy.  $Hv$  represents the Vickers microhardness,  $H_0$  is the stress of friction in terms of hardness,  $k$  is a constant,  $d$  is the TEM grain size,  $\alpha$  is a constant (0.3),  $M$  is factor of Taylor (3),  $G$  is the modulus of shear (26 GPa),  $b$  is the vector of Burgers (0.286 nm) and  $\rho$  is the density of dislocation that computed by XRD. The results calculated from both Hall–Petch and Taylor were normalized by the experimental recorded hardness in a similar manner to a recent study [21], then these results are plotted in Fig. 14 in order to show the distinct (separate) contributions of grain size and dislocation density on the resultant strengthening.

## Discussion

### Microstructure morphology and grain refinement

The microstructure of the additive manufactured Al-9%Si-3%Cu aluminium alloy was significantly refined into nanoscale grain sizes by HPT at room temperature as showed in the OM, SEM and TEM observations (Figs. 2, 3, 4, 6). High-pressure torsion has introduced significant alteration in the microstructure morphology, grain size and density of dislocations in the alloy after processing. These changes were indicated via the refinement of  $\alpha$ -Al matrix, fragmentation and uniform distribution of Si eutectic phase (Fig. 5), and accumulation of high density of dislocations within the refined microstructure (Fig. 13).

The HPT processing has changed the microstructure morphology from the large melt-pool

morphology to ultrafine grains (Fig. 2). This is ascribed to the influence of torsional shear strain imposed by the HPT that has resulted in refinement of the grains inside the melt pools, rotation of the grains in the direction of torsional shear strain, disappearance of the melt pools and finally generation of ultrafine grains as the torsional deformation proceeded. This is consistent with many previous investigations [3, 15, 29]. It was shown that the two-phases materials processed by HPT to exhibit shear vortices phenomenon [30–33]. These local vortices structures appear at a high level of strain HPT deformation, where the plastic flow of the processed material is variable from one region to another on the processed HPT disk due to heterogenous distribution of HPT strain between the centre and edge regions. The visualization of strain heterogeneity is affected by the amount of phases in processed material, where a two-phases material with high percentage of both phases and different plasticity would show more visual vortices during HPT such as in 50% asutentic-50% ferrite duplex steel [30, 31], Cu-28%Ag alloy [32] bronze/niobium composite [33]. In the current processed alloy, the amount of the second phase (silicon) was about 9% within the alloy, thus less visualization of these vortices was observed compared to the aforementioned investigations especially at the preliminary stage of HPT deformation. These vortices were observed at the high number of turns (10 turns) at the central regions of the processed disk as shown in Fig. 2c. These vortices were assumed to be driven primarily by the local plastic instability that arises from the localized blocking of shear deformation at the central regions of HPT-processed samples. Agglomeration of fine precipitates and second-phase particles could cause such localized deformation blockage and heterogeneity distribution of the shear strain, which can be estimated through minor difference in the microhardness distribution at the central regions compared to the peripheral regions of HPT-processed samples [33–35]. Therefore, these vortices were seen clearly on the centre regions over horizontal cross sections (Fig. 2c) and along the whole vertical cross sections (Fig. 2f) in the processed sample for 10 turns.

Grain refinement has happened extensively in the additively manufactured alloy in the preliminary stages of the HPT deformation where the average value of grain size has reached 60 nm (Fig. 6c) and the average value of eutectic particle size decreased

**Figure 2** OM observations over the *horizontal* cross sections of the disks at central regions showing: (a and b) polished and etched as-received samples and c processed sample for 10 turns. The OM observations over the *vertical* cross sections of the disks showing: d as-received sample, e and f processed sample for 10 turns at the central and peripheral regions, respectively.

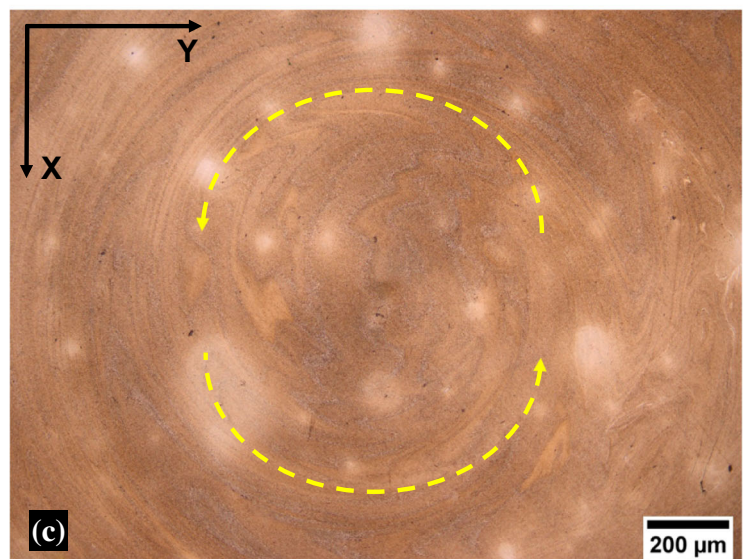
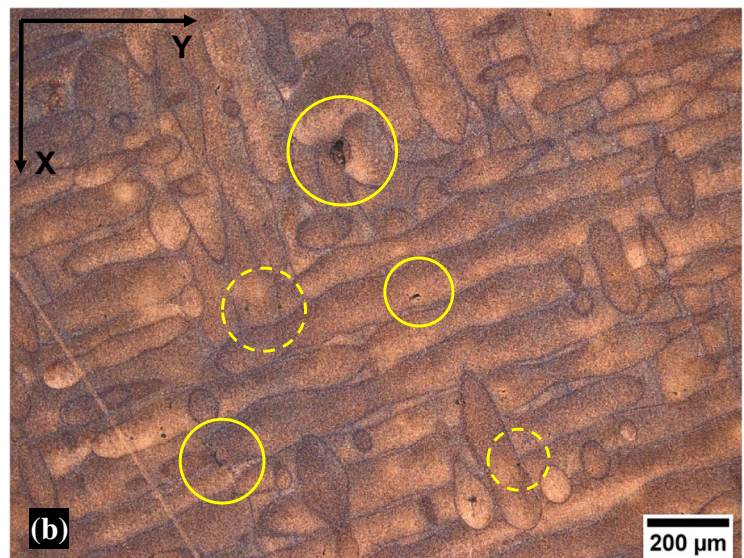
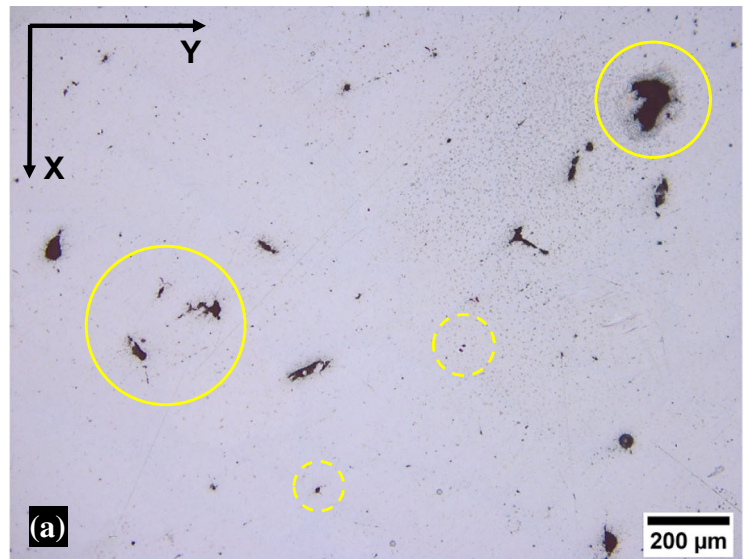
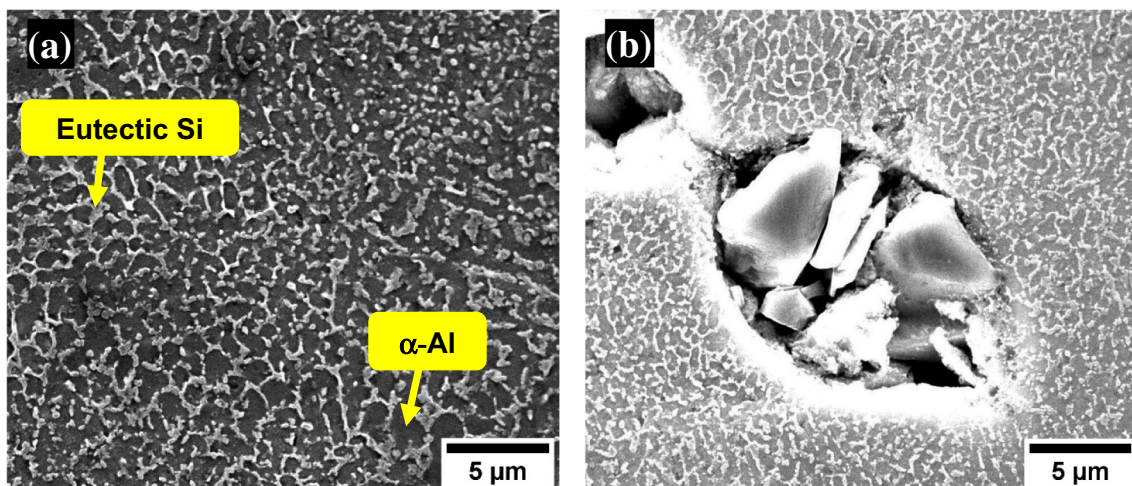
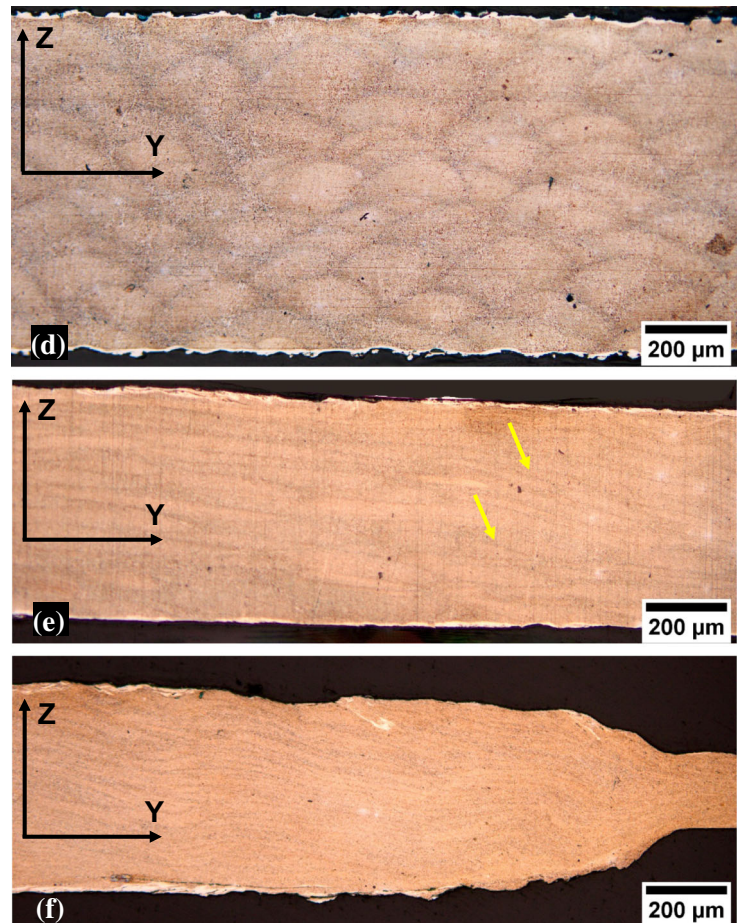


Figure 2 continued.



**Figure 3** SEM observations of the as-received sample showing: **a** the initial microstructure, **b** the lack-of-fusion porosity over the horizontal cross sections of the disks.

to 175 nm after 10 turns (Fig. 5). Formation of subgrains observed in the processed sample up to 10 turns (Fig. 6c) could be ascribed to the dislocation accumulation and tangling in these dark contrast

areas [36]. The deformation-induced twinning on Si eutectic plane (220) [37, 38] has provided deformation continuity from the relatively ductile  $\alpha$ -Al matrix to the brittle Si eutectic phase under such heavy HPT

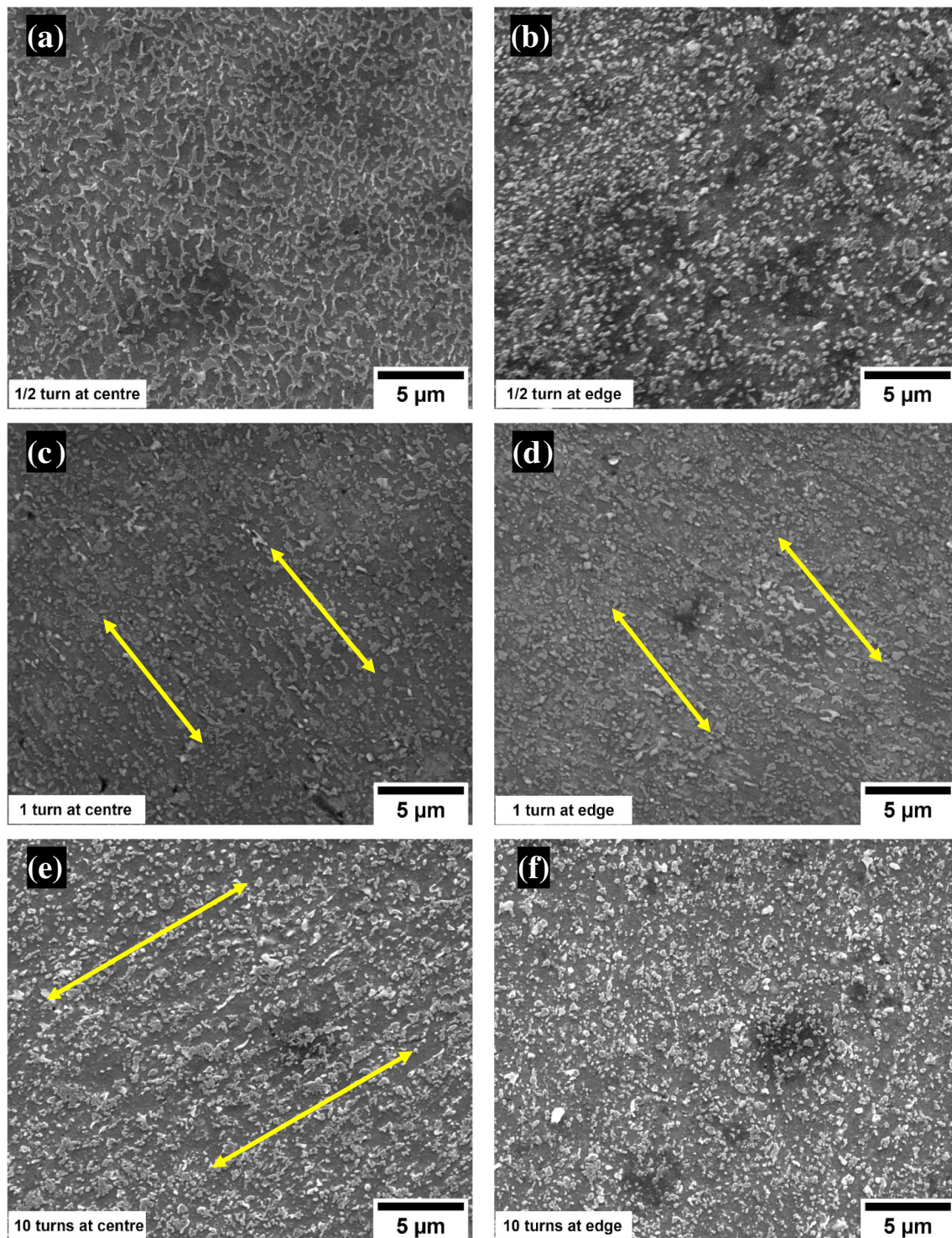


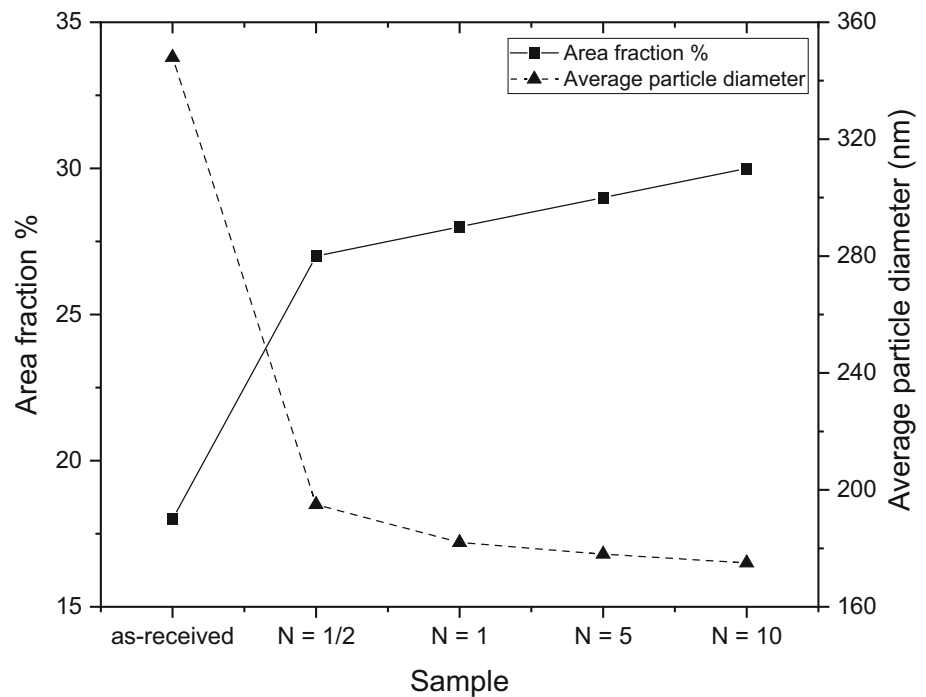
**Figure 4** SEM observations of the processed samples at various HPT turns over the *horizontal* cross sections of the processed disks.

imposed strains [39]. The existence of deformation-induced twinning was assumed to occur across the  $\alpha$ -Al matrix/Si eutectic phase interfaces of different crystallographic orientation [40]. This interface plays a role in strengthening the microstructure, where the

accumulation of moving dislocations via the Al/Si interface during HPT deformation contributes to additional strengthening in the processed alloy [41, 42].



**Figure 5** Distribution of area fraction and average particle diameter for the eutectic Si phase for the as-received and processed samples at various HPT turns.



A finer microstructure has been obtained in the additively manufactured Al-9%Si-3%Cu alloy compared to the as-cast Al-7%Si alloy processed using HPT where grain size of 300–700 nm is reported [43], or in as-cast Al-11%Si-1%Cu alloy processed using ECAP with a reported grain size of 200–400 nm [44], or as-cast Al-7%Si alloy processed using HPT with a reported grain size of 87 nm [45]. This can be attributed to the initial microstructure of the current alloy compared to these counterparts. The as-cast Al-7%Si alloy was prepared from casting of pure aluminum with master Al-Si alloy with relatively large initial grain size of 50  $\mu\text{m}$ , and then a relatively lower strain was imposed via only 5 turns in HPT [43]. However, the current alloy has been processed using 10 turns at the same applied pressure for both alloys that indicates the direct impact of imposed strain on the extent of the grain refinement [18].

It is familiar that the imposed strain by HPT is larger compared to ECAP, therefore, a finer microstructure with larger dislocation density is expected compared to that using ECAP as seen in this investigation when compared to the as-cast Al-11%Si-1%Cu alloy [18, 46, 47]. The ratios of silicon and copper in the Al-Si-Cu alloy have influence on the level of grain refinement. These elemental additions are expected to decrease the stacking fault energy for the alloy and activate deformation-induced twinning

and dislocation structures resulting in an increase in grain refinement [48, 49]. Therefore, the current Al-9%Si-3%Cu has achieved a finer microstructure than an Al-7%Si alloy despite the HPT applied pressure being relatively lower (6 GPa) in the current work compared to the counterpart work (8 GPa) that was used for the Al-7%Si alloy, which indicates the important role of alloying elements in grain refinement processes over simply considering the HPT applied pressure [38, 50]. The grain refinement observed by TEM is relatively consistent with the crystallite size data obtained by XRD measurements (Fig. 12), which confirms the effectiveness of HPT processing at room temperature in the additively manufactured Al-9%Si-3%Cu alloy.

The processed alloy has undergone considerable deformation that has been stored within the microstructure in the form of lattice distortions, which was detected as broadening and shifting in the XRD peaks in the processed samples for different numbers of HPT turns (Fig. 7b) [51, 52]. The HPT deformation has caused a shift to the lower diffraction angles that led to an increase in the lattice spacings and microstrain values as shown in Fig. 7d. This expansion in the distorted lattices can be attributed to the presence of tensile strains within these lattices due to potential interstitials of ultrafine precipitates of intermetallic phases and deformation-

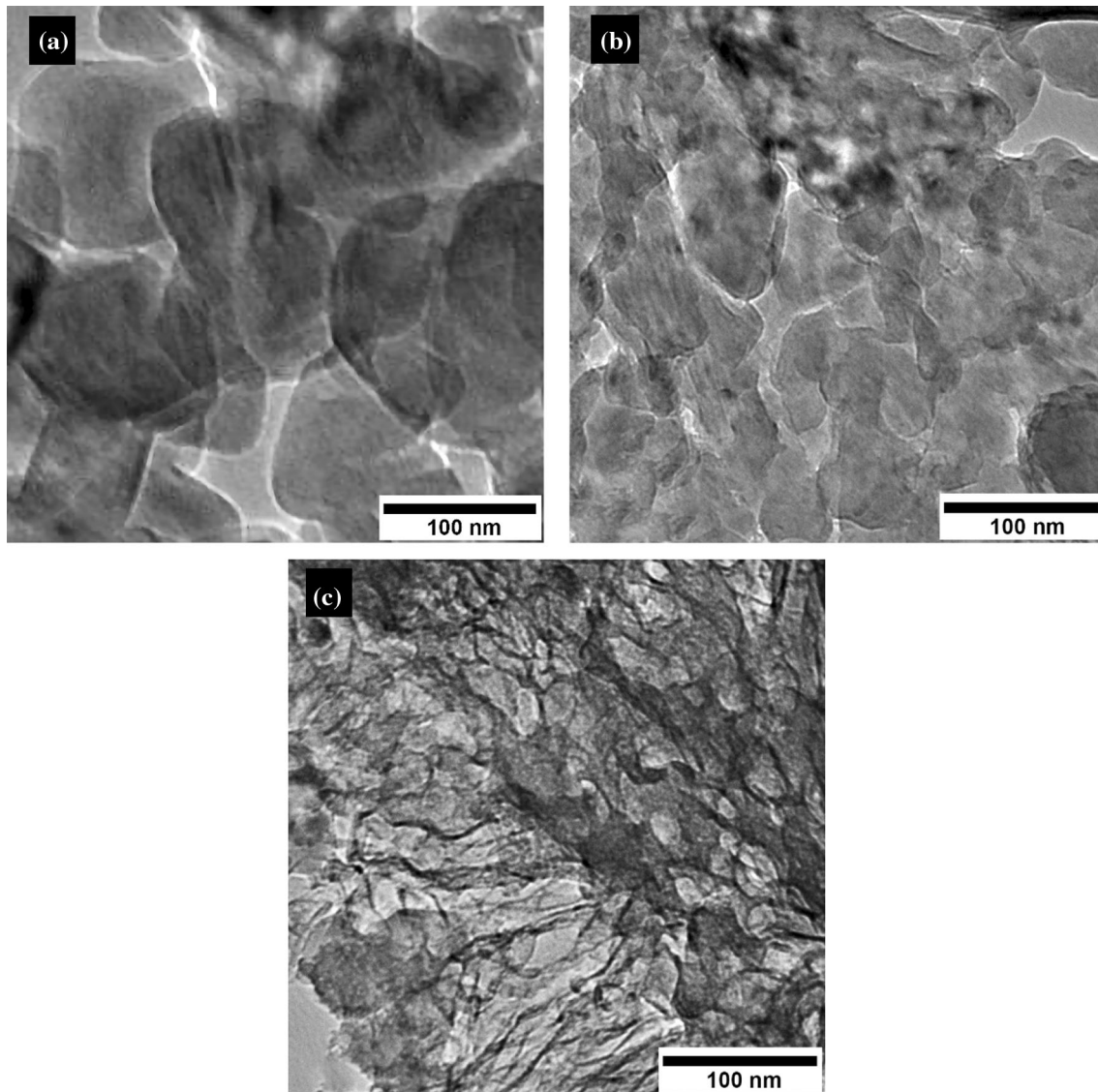


**Figure 6** TEM observations of the processed samples for: **a** 1/2 turn, **b** 1 turn, and **c** 10 turns.

induced twinning within the crystallographic planes, as well as the lattice curvature due to the heavy dislocation density [53–55]. However, the expansion in the distorted lattices has been found to reduce the stacking fault energy, thus leading to occurrence of deformation-induced twinning that contribute to strengthening in the processed alloy [56–58].

### Porosity elimination

The as-received sample contained (1) gas-induced and (2) process-induced porosities. (1) has a spherical shape, as observed in the OM micrographs (Fig. 2a, b) and arises from gas molecule dissolution into the melt powders during the additive manufacturing

process, and then their re-nucleation on cooling. (2) tends to have irregular shapes as seen in OM micrographs and occurs due to lack-of-fusion in some areas of the powders due to inadequate fusion in these spots and/or spattering of powders from these spots by the high vapor pressure of the melt [1]. A significant porosity reduction has been achieved in the HPT processed additive manufactured alloy as indicated by Archimedes and ImageJ analysis procedures (Figs. 8, 9).

This reduction in porosity has been observed in the processed samples across the horizontal and vertical cross sections. Several factors in HPT processing have controlled the porosity reduction: hydrostatic

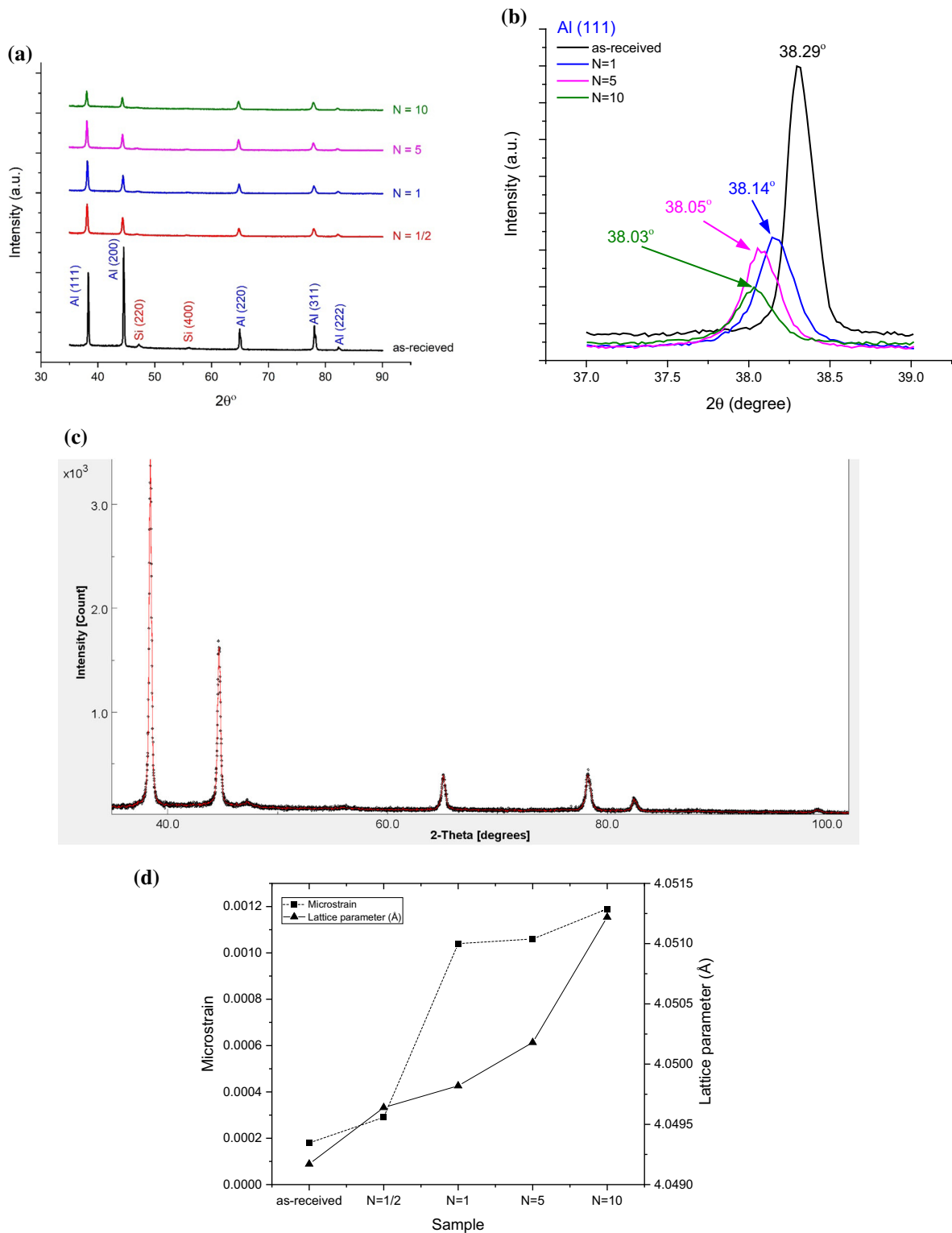


**Figure 7** **a** Patterns of XRD in the as-received and processed samples at various HPT turns, **b** Magnified part of (a) showing peak shifting, **c** the scattered data are the XRD profile for the alloy

and the solid colorful line profile is the Rietveld fitted data, and **d** the variation in the microstrain and lattice parameter in the as-received and processed samples.

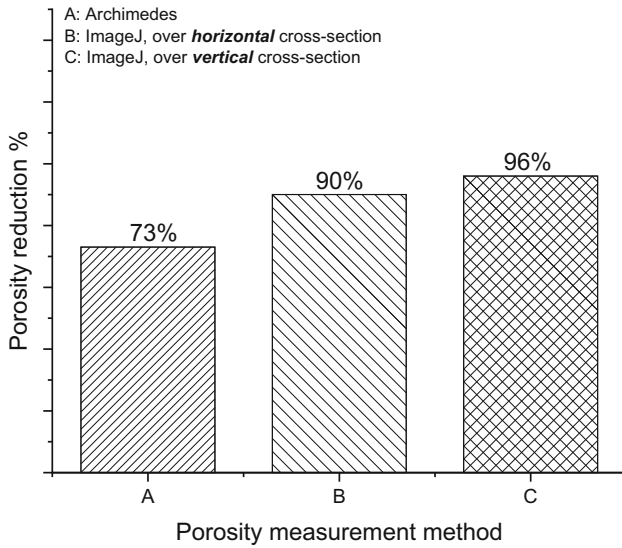


**Figure 8** Porosity reduction percentages as calculated by different procedures for the processed sample at 10 turns compared to the as-received sample.

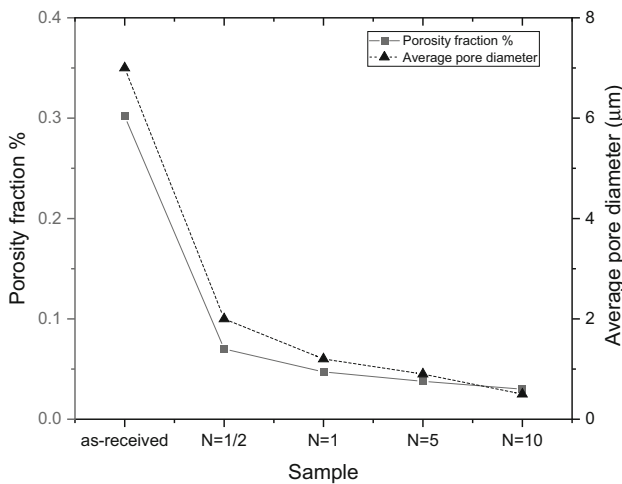


**Figure 9** Porosity fraction and average pore diameter data of the as-received and processed samples at edge regions of HPT disks.

pressure and torsional shear strain. The hydrostatic pressure is due to the state of stress when the alloy comes into contact with anvils. This pressure contributes to prevent cracking and then confines the material under processing, thus enhancing the solidity of the processed microstructure [59, 60]. It has been shown that increasing HPT pressure has resulted in reduction in the interconnected porosity in pure copper up to 6 GPa [61].

The current alloy was processed at 6GPa producing several microstructural features that also contributed to coalescence of pre-existing voids and pores during

HPT torsional deformation. The morphology of both matrix and eutectic phases was altered significantly as the torsional shear strain increased, as observed in OM and SEM micrographs (Figs. 2, 3, 4). The torsional HPT strain has contributed to microstructural reorientation and refinement including  $\alpha$ -Al and eutectic Si phase, which has resulted in filling the pores as the torsional strain increases with number of turns [3, 18, 62, 63]. The microstructural evolution leads to pore closure, the reduction in porosity fraction and pore diameter occur at a relatively faster rate at the peripheral areas than the central region of the deformed disks as a result of the HPT imposed strain being higher at the peripheries than the central regions of the disk [3, 18, 19]. It was found that HPT has an effective impact on vacancy annihilation and then porosity elimination by means of rearrangement of dislocation structures [60, 64].

The difference in porosity data between Archimedes and ImageJ analysis procedures (Fig. 8) can be attributed to the nature of each test regarding the porosity counting. In Archimedes method, the closed pores inside the alloy were not filled with the immersion liquid leading to inaccurate volume measurement. This exclusion of closed pores has resulted in the difference of porosity data between Archimedes and ImageJ analysis [65, 66]. However, a relatively higher consistency between the aforementioned procedures was obtained with the higher HPT deformation, where more pores closure is expected to occur under the conditions of severe HPT pressure and torsion [3]. Both procedures taken together have provided a reliable estimation of porosity and density of the additive manufactured alloy combining the impact of the total volume of sample considered and different cross sections under imaging [23, 67].

### Strength evolution

The evolution in strength of the additive manufactured Al–Si–Cu alloy after HPT processing was expressed in terms of hardness development. The microstructural heterogeneity in the processed samples at a comparatively low number of HPT turns has caused a diversity in the microhardness distribution (Figs. 10, 11). The gradual increasing homogeneity in the strength was achieved using additional HPT straining at higher turns, because of a progressive development of microstructural homogeneity in the

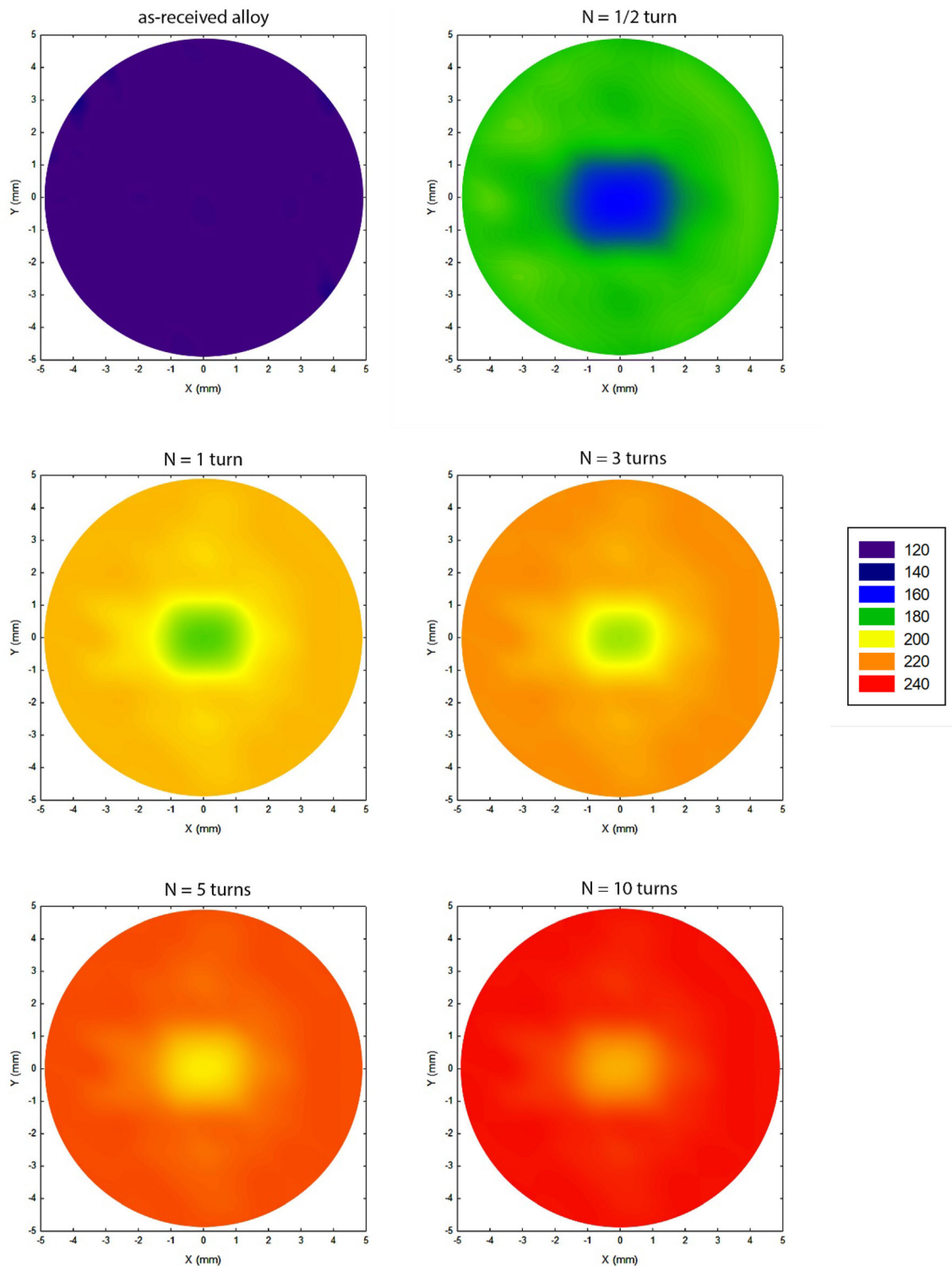


**Figure 10** Color-coded hardness maps for the as-received and processed samples over the *horizontal* cross sections.

HPT processed samples over the horizontal and vertical cross sections [18, 29, 45].

A higher HPT imposed strain has contributed to microstructural and strength homogeneity in the

through-thickness direction of the HPT samples [18, 68]. The Al-9%Si-3%Cu additively manufactured alloy has showed a comparatively higher level of strengthening than the Al-7%Si, where all

**Figure 11** Color-coded hardness maps for the as-received and processed samples over the *vertical* cross sections.

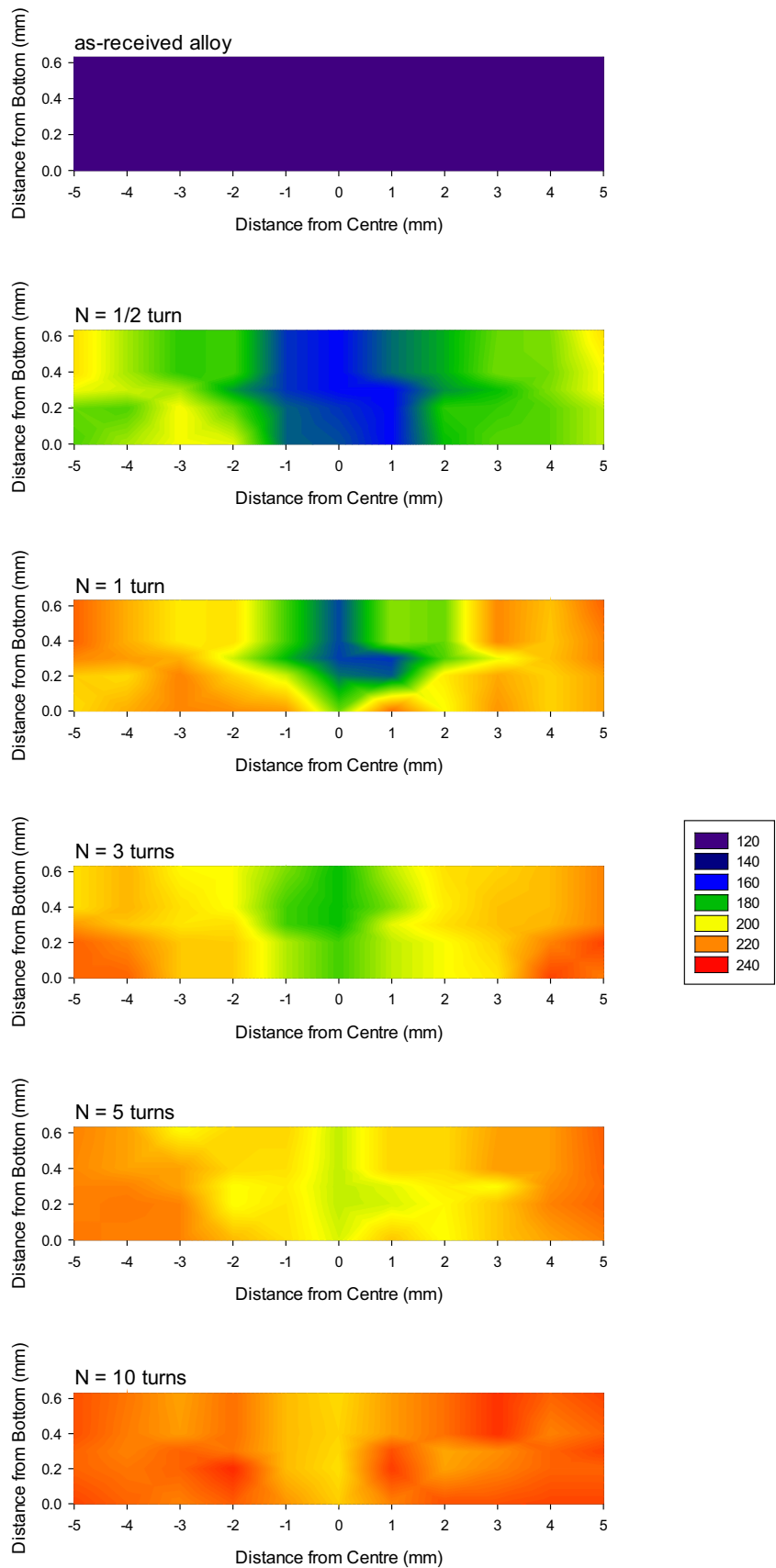


**Figure 12** Variation in the crystallite size, grain size and hardness with the HPT turns.

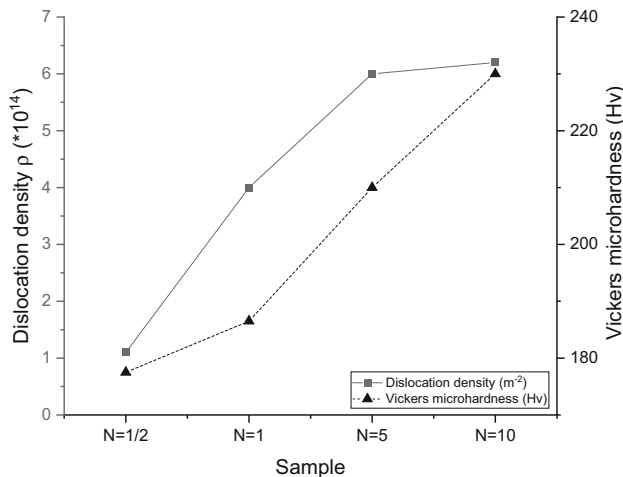
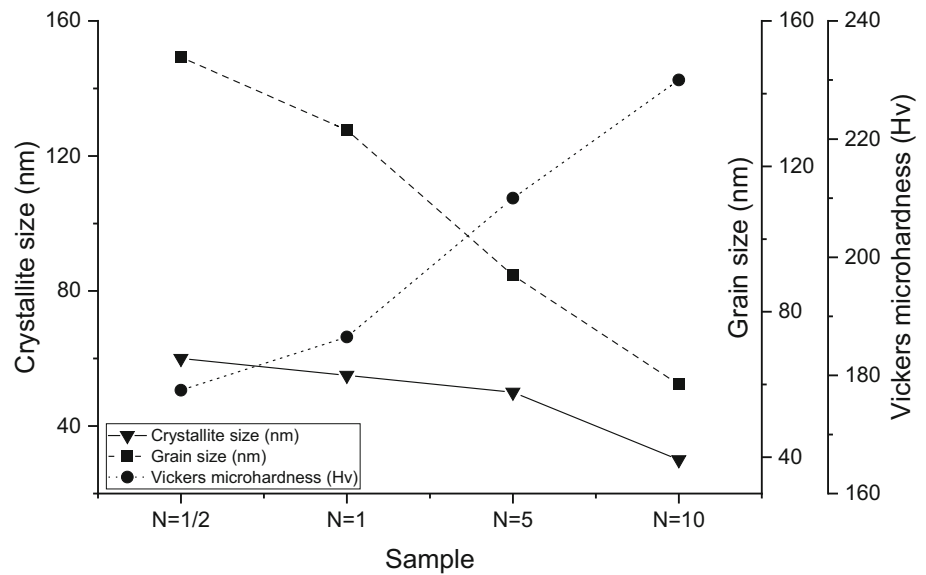


**Figure 13** Variation in the dislocation density and hardness with the HPT turns.

mentioned alloys were processed by HPT [45, 57]. This can be ascribed mainly to the level of grain refinement, dislocation density and existence of second-phase fine particles. A high fraction of high-angle grain boundaries will be generated with the progress of the torsional straining, which will restrict the dislocation motion during plastic deformation, resulting in strengthening of the microstructure [18, 28, 69].

The Al-9%Si-3%Cu additively manufactured alloy has exhibited smaller ultrafine-grain microstructure and higher strength rather than the Al-7%Si alloy, which reflects the dependence of strengthening effect on grain size reduction (Figs. 12, 13). The

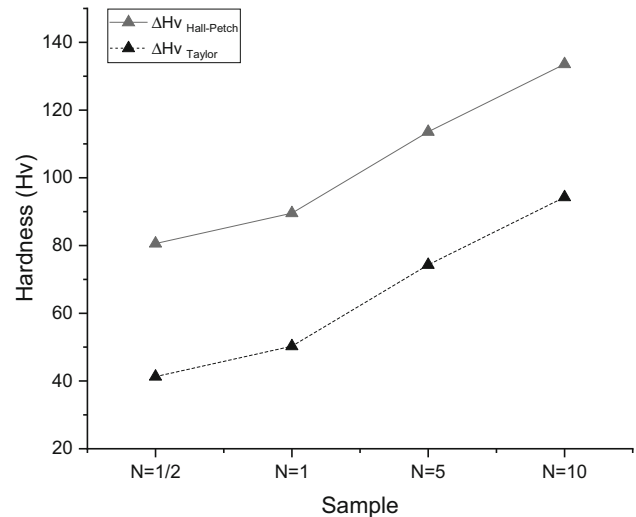


**Figure 14** A comparison between the grain boundary strengthening as expressed by the calculated hardness from Hall–Petch equation and the dislocation strengthening as expressed by the calculated hardness from Taylor equation.

improvement in strength of the processed alloy was associated with the progress of equivalent imposed strain [18, 69]. The dependency of strength on grain size for the alloy was expressed using Hall–Petch using hardness and TEM grain size data [70, 71],  $H_v(\text{MPa}) = 945 + 325d^{-1/2}$ , where  $H_o = 945\text{MPa}$  and  $k_H = 325\text{MPa}\cdot\mu\text{m}^{-1/2}$ . These high values indicate the significant grain refinement and dislocation density effect on the strength of the processed alloy [72, 73].

The strengthening in the current HPT-processed additive manufactured alloy was achieved mainly by

the grain refinement and dislocation activity as calculated by the Hall–Petch and Taylor relationships, respectively. Hall–Petch relationship refers to the strengthening from grain boundaries that act as obstacles for dislocation motion [74–76]. Taylor relationship describes strengthening by dislocation–dislocation interactions during accumulation at the grain boundaries [28, 77]. By comparison of the calculated strengthening from the grain size reduction and dislocation activity as presented in Fig. 14, it is clear that the grain boundaries have a relatively larger impact on the strengthening rather than the dislocation forest. The remaining contribution to the strengthening is inferred to have come from the pinning and accumulation of moving dislocations at the nano-sized particles of the Si eutectic phase [28, 63, 77].

At low HPT strains, the dislocation–dislocation interactions are generally considered to be more effective in strengthening which is associated with lower misorientation between the grain boundaries. At higher HPT strains, the obstacle resistance of grain boundaries is considerable and increases with higher misorientation between the grain boundaries [28, 47, 78]. However, the current processed alloy showed a significant grain refinement at the preliminary stages of HPT deformation that caused a dominating effect by strengthening from the grain boundaries over the dislocation–dislocation interactions [20, 28]. The current data showed a clear dependency of the strength on both TEM estimated grain size and density of dislocation observed in the deformed alloy. However, the calculations of crystallite size were obtained with some potential errors compared to the TEM grain size data, that could be the reason for the minor difference between the aforementioned mechanisms [27, 28, 79].

A substantial dislocation density has been achieved in the processed samples on increasing the HPT torsional straining up to 10 turns. Dislocation density has accumulated effectively in the processed alloy under room temperature-HPT rather than elevated temperature-HPT [18, 19, 80, 81]. There are many factors that could affect the evolution of dislocations during HPT processing: applied HPT pressure, volume fraction of the nano-sized particles and stacking fault energy [18, 19].

An increase in the HPT pressure obstructs the migration of defects that suppresses the annihilation of these defects [64, 82]. It was found that fragmentation and distribution of second phase particles of

nano-sizes within the processed microstructure have resulted in additional obstruction of the dislocations' motion [41, 83]. In this research, considerable refinement and distribution in the Si eutectic phase during HPT were associated with relatively homogeneous distribution of these eutectic nano-sized particles over the whole of the processed samples. This behavior of the second phase provides an additional strengthening of the processed alloy when tested at room temperature and enhances the superplastic performance at higher temperatures [17, 84].

Stacking fault energy of pure aluminium is normally high and relatively lower for its alloys, thus addition of alloying elements has shown a reduction in this energy resulting in easier formation of partial dislocations and deformation-induced twinning [85, 86]. The current alloy has silicon, copper and magnesium as alloying elements which not only reduce the stacking fault energy of aluminum, but also provide additional sources for dislocations and thus strengthening [87, 88]. The high contents of Si and of Cu in the Al-9%Si-3%Cu compared with the Al-7%Si have another impact on strengthening in the current processed alloy. These elements normally form several hard intermetallic phases (such as  $\text{Al}_2\text{Cu}$  and  $\text{Al}_8\text{Fe}_2\text{Si}$ ) in addition to the eutectic Si [89, 90].

As a result, the volume fractions of these phases in the Al-9%Si-3%Cu alloy are higher than in Al-7%Si alloy. The alloying elements were added in relatively precise manner during the direct laser melting process, which is considered as a controllable-microstructure manufacturing process. Therefore, all these elemental structures were subjected to extensive refinement down to nanoscale during HPT and acted as barriers to dislocations motion. Accordingly, the strengthening in the Al-9%Si-3%Cu alloy has increased with the higher volume fractions of these hard nano-sized secondary phases after HPT [91–93].

The increment in volume fraction of the eutectic nano-sized particles with progress in torsional HPT deformation will result in a reduction in the mean free path of the accumulated dislocations. Therefore, more barriers for dislocation mobility will appear that would improve the strength [73, 94, 95]. A similar trend of increasing the dislocation density has been found with increasing the fraction of alloying element in the additively manufactured alloys Al-3.5%Si-1.5%Mg and Al-3.5%Si-2.5%Mg [81]. A comparison of the current HPT processed Al–Si–Cu alloy with a Al–Si–Cu/SiC alloy composite subjected to



HPT [96], revealed that the current processed additively manufactured alloy has a comparable strength without addition of SiC hard particles. This also indicates the impact of combination of severe plastic deformation with controllable-microstructure additively manufactured alloy.

## Conclusions

1. Effective grain refinement (60 nm) and dislocation density ( $6.2 \times 10^{14} \text{ m}^{-2}$ ) have been obtained by room temperature-HPT processing at higher HPT turns (10 turns) for the additively manufactured Al-9%Si-3%Cu alloy.
2. A considerable porosity reduction has been measured via Archimedes method (75%) and image analysis (96%) at higher HPT turns (10 turns) and linked to the hydrostatic pressure and torsional deformation.
3. Strength homogeneity was obtained over both horizontal and vertical cross sections at higher HPT turns (10 turns), which is attributed to the evolution in microstructural homogeneity with further HPT deformation.
4. The ultrafine-grained additively manufactured alloy showed a good consistency between the grain size and dislocation strengthening mechanisms. The content of alloying elements, nano-sized and distribution of second-phase particles have additional effects on the resultant strengthening.

## Acknowledgements

This work was supported by the Ministry of Higher Education and Scientific Research and University of Technology (Iraq), as well as the University of Southampton, School of Engineering (UK). The author (Ahmed S.J. Al-Zubaydi) is appreciative to Prof. Philippa A.S. Reed and Dr. Nong Gao for their support.

## Author's contribution

Ahmed S.J. Al-Zubaydi contributed to formal analysis, methodology, Writing—original draft, investigation. Philippa A.S. Reed & Nong Gao contributed to

supervision, conceptualization, writing—review & editing.

## Declaration

**Conflict of interest** The authors state that they have no competing financial interests or known personal relationships that could appear to affect the work presented in this article.

**Open Access** This article is licensed under a Creative Commons Attribution 4.0 International License, which permits use, sharing, adaptation, distribution and reproduction in any medium or format, as long as you give appropriate credit to the original author(s) and the source, provide a link to the Creative Commons licence, and indicate if changes were made. The images or other third party material in this article are included in the article's Creative Commons licence, unless indicated otherwise in a credit line to the material. If material is not included in the article's Creative Commons licence and your intended use is not permitted by statutory regulation or exceeds the permitted use, you will need to obtain permission directly from the copyright holder. To view a copy of this licence, visit <http://creativecommons.org/licenses/by/4.0/>.

## References

- [1] Aboulkhair NT, Simonelli M, Parry L, Ashcroft I, Tuck C, Hague R (2019) 3D printing of Aluminium alloys: additive manufacturing of aluminium alloys using selective laser melting. *Prog Mater Sci* 106:100578. <https://doi.org/10.1016/j.pmatsci.2019.100578>
- [2] Hosseinzadeh A, Radi A, Richter J, Wegener T, Sajadifar SV, Niendorf T, Yapici GG (2021) Severe plastic deformation as a processing tool for strengthening of additive manufactured alloys. *J Manuf Process* 68:788–795. <https://doi.org/10.1016/j.jmapro.2021.05.070>
- [3] Yusuf SM, Hoegden M, Gao N (2020) Effect of sample orientation on the microstructure and microhardness of additively manufactured AlSi10Mg processed by high-pressure torsion. *Int J Adv Manuf Technol* 106:4321–4337. <https://doi.org/10.1007/s00170-019-04817-5>
- [4] Thijs L, Kempen K, Kruth JP, Van Humbeeck J (2013) Fine-structured aluminium products with controllable texture by selective laser melting of pre-alloyed AlSi10Mg powder. *Acta Mater* 61:1809–1819. <https://doi.org/10.1016/j.actamat.2012.11.052>

- [5] Fousova M, Dvorsky D, Vronka M, Vojtech D, Lejcek P (2018) The use of selective laser melting to increase the performance of AlSi9Cu3Fe alloy. *Materials* (Basel) 11:1918. <https://doi.org/10.3390/ma11101918>
- [6] Li XP, Wang XJ, Saunders M, Suvorova A, Zhang LC, Liu YJ, Fang MH, Huang ZH, Sercombe TB (2015) A selective laser melting and solution heat treatment refined Al-12Si alloy with a controllable ultrafine eutectic microstructure and 25% tensile ductility. *Acta Mater* 95:74–82. <https://doi.org/10.1016/j.actamat.2015.05.017>
- [7] Ma P, Jia Y, Prashanth KG, Scudino S, Yu Z, Eckert J (2016) Microstructure and phase formation in Al-20Si-5Fe-3Cu-1Mg synthesized by selective laser melting. *J Alloys Compd* 657:430–435. <https://doi.org/10.1016/j.jallcom.2015.10.119>
- [8] Nandy J, Sarangi H, Sahoo S (2018) Microstructure evolution of Al-Si-10Mg in direct metal laser sintering using phase-field modeling. *Adv Manuf* 6:107–117. <https://doi.org/10.1007/s40436-018-0213-1>
- [9] Ghosh SK, Saha P, Kishore S (2010) Influence of size and volume fraction of SiC particulates on properties of ex situ reinforced Al-4.5Cu-3Mg metal matrix composite prepared by direct metal laser sintering process. *Mater Sci Eng A* 527:4694–4701. <https://doi.org/10.1016/j.msea.2010.03.108>
- [10] Ye H (2003) An overview of the development of Al-Si-alloy based material for engine applications. *J Mater Eng Perform* 12:288–297. <https://doi.org/10.1361/105994903770343132>
- [11] Fiocchi J, Biffi CA, Tuissi A (2020) Selective laser melting of high-strength primary AlSi9Cu3 alloy: processability, microstructure, and mechanical properties. *Mater Des* 191. <https://doi.org/10.1016/j.matdes.2020.108581>
- [12] Barbosa J, Puga H, Oliveira J, Ribeiro S, Prokic M (2014) Physical modification of intermetallic phases in Al–Si–Cu alloys. *Mater Chem Phys* 148:1163–1170. <https://doi.org/10.1016/j.matchemphys.2014.09.041>
- [13] Yildirim M, Özyürek D (2013) The effects of Mg amount on the microstructure and mechanical properties of Al-Si-Mg alloys. *Mater Des* 51:767–774. <https://doi.org/10.1016/j.matdes.2013.04.089>
- [14] Ngo TD, Kashani A, Imbalzano G, Nguyen KTQ, Hui D (2018) Additive manufacturing (3D printing): A review of materials, methods, applications and challenges. *Compos Part B Eng* 143:172–196. <https://doi.org/10.1016/j.compositesb.2018.02.012>
- [15] Mohd Yusuf S, Nie M, Chen Y, Yang S, Gao N (2018) Microstructure and corrosion performance of 316L stainless steel fabricated by Selective Laser Melting and processed through high-pressure torsion. *J Alloys Compd* 763:360–375. <https://doi.org/10.1016/j.jallcom.2018.05.284>
- [16] Zhao W, Han J-K, Kuzminova YO, Evlashin SA, Zhilyaev AP, Pesin AM, Jang J, Liss K-D, Kawasaki M (2021) Significance of grain refinement on micro-mechanical properties and structures of additively-manufactured CoCr-FeNi high-entropy alloy. *Mater Sci Eng A* 807:140898. <https://doi.org/10.1016/j.msea.2021.140898>
- [17] Al-Zubaydi ASJ, Zhilyaev AP, Wang SC, Reed PAS (2015) Superplastic behaviour of AZ91 magnesium alloy processed by high-pressure torsion. *Mater Sci Eng A* 637:1–11. <https://doi.org/10.1016/j.msea.2015.04.004>
- [18] Zhilyaev AP, Langdon TG (2008) Using high-pressure torsion for metal processing: fundamentals and applications. *Prog Mater Sci* 53:893–979. <https://doi.org/10.1016/j.pmatsci.2008.03.002>
- [19] Al-Zubaydi ASJ, Zhilyaev AP, Wang SC, Kucita P, Reed PAS (2016) Evolution of microstructure in AZ91 alloy processed by high-pressure torsion. *J Mater Sci* 51:3380–3389. <https://doi.org/10.1007/s10853-015-9652-2>
- [20] Mohd Yusuf S, Chen Y, Yang S, Gao N (2020) Microstructural evolution and strengthening of selective laser melted 316L stainless steel processed by high-pressure torsion. *Mater Charact* 159:110012. <https://doi.org/10.1016/j.matchar.2019.110012>
- [21] Gubicza J, El-Tahawy M, Lábár JL, Bobruk EV, Murashkin MY, Valiev RZ, Chinh NQ (2020) Evolution of microstructure and hardness during artificial aging of an ultrafine-grained Al-Zn-Mg-Zr alloy processed by high pressure torsion. *J Mater Sci* 55:16791–16805. <https://doi.org/10.1007/s10853-020-05264-4>
- [22] Vander Voort, Baldwin W (2004) *Metallography and microstructures handbook*. ASM Int 9:2733. <http://www.worldcat.org/oclc/42469467>
- [23] Spierings AB, Schneider M, Eggenberger R (2011) Comparison of density measurement techniques for additive manufactured metallic parts. *Rapid Prototyp J* 17:380–386. <https://doi.org/10.1108/13552541111156504>
- [24] de Terris T, Andreau O, Peyre P, Adamski F, Koutiri I, Gorny C, Dupuy C (2019) Optimization and comparison of porosity rate measurement methods of Selective Laser Melted metallic parts. *Addit Manuf* 28:802–813. <https://doi.org/10.1016/j.addma.2019.05.035>
- [25] Cai X, Malcolm AA, Wong BS, Fan Z (2015) Measurement and characterization of porosity in aluminium selective laser melting parts using X-ray CT. *Virtual Phys Prototyp* 10:195–206. <https://doi.org/10.1080/17452759.2015.1112412>
- [26] ASTM E562-19e1, Standard test method for determining volume fraction by systematic manual point count, 2011. <https://doi.org/10.1520/E0562-19E01>
- [27] Ribárik G, Gubicza J, Ungár T (2004) Correlation between strength and microstructure of ball-milled Al-Mg alloys determined by X-ray diffraction. *Mater Sci Eng A*

- 387–389:343–347. <https://doi.org/10.1016/j.msea.2004.01.089>
- [28] Gubicza J, Chinh NQ, Krállics G, Schiller I, Ungár T (2006) Microstructure of ultrafine-grained fcc metals produced by severe plastic deformation. *Curr Appl Phys* 6:194–199. <https://doi.org/10.1016/j.cap.2005.07.039>
- [29] Al-Zubaydi A, Figueiredo RB, Huang Y, Langdon TG (2013) Structural and hardness inhomogeneities in Mg-Al-Zn alloys processed by high-pressure torsion. *J Mater Sci* 48:4661–4670. <https://doi.org/10.1007/s10853-013-7176-1>
- [30] Cao Y, Wang YB, Alhajeri SN, Liao XZ, Zheng WL, Ringer SP, Langdon TG, Zhu YT (2010) A visualization of shear strain in processing by high-pressure torsion. *J Mater Sci* 45:765–770. <https://doi.org/10.1007/s10853-009-3998-2>
- [31] Huang Y, Kawasaki M, Al-Zubaydi A, Langdon TG (2014) Effect of anvil roughness on the flow patterns and hardness development in high-pressure torsion. *J Mater Sci* 49:6517–6528. <https://doi.org/10.1007/s10853-014-8203-6>
- [32] Tian YZ, An XH, Wu SD, Zhang ZF, Figueiredo RB, Gao N, Langdon TG (2010) Direct observations of microstructural evolution in a two-phase Cu-Ag alloy processed by high-pressure torsion. *Scr Mater* 63:65–68. <https://doi.org/10.1016/j.scriptamat.2010.03.014>
- [33] Rogachev SO, Nikulin SA, Khatkevich VM, Sundeev RV, Kozlov DA (2019) High-pressure torsion deformation process of bronze/niobium composite. *Trans Nonferrous Met Soc China* 29:1689–1695. [https://doi.org/10.1016/S1003-6326\(19\)65075-2](https://doi.org/10.1016/S1003-6326(19)65075-2)
- [34] Jiang W, Zhou H, Cao Y, Nie J, Li Y, Zhao Y, Kawasaki M, Langdon TG, Zhu Y (2020) On the heterogeneity of local shear strain induced by high-pressure torsion. *Adv Eng Mater* 22:14–16. <https://doi.org/10.1002/adem.201900477>
- [35] Kulagin R, Beygelzimer Y, Ivanisenko Y, Mazilkin A, Straumal B, Hahn H (2018) Instabilities of interfaces between dissimilar metals induced by high pressure torsion. *Mater Lett* 222:172–175. <https://doi.org/10.1016/j.matlet.2018.03.200>
- [36] Ma R, Peng C, Cai Z, Wang R, Zhou Z, Li X, Cao X (2020) Enhanced strength of the selective laser melted Al-Mg-Sc-Zr alloy by cold rolling. *Mater Sci Eng A* 775:138975. <https://doi.org/10.1016/j.msea.2020.138975>
- [37] Zhai S, Zhang C, Zhou N, Huang L, Lin M, Zhou L (2019) The twin formations on different growth planes of silicon crystal growth from melt by a molecular dynamics study. *Phys B Condens Matter* 572:184–189. <https://doi.org/10.1016/j.physb.2019.07.031>
- [38] Gwalani B, Olszta M, Varma S, Li L, Soulami A, Kautz E, Pathak S, Rohatgi A, Sushko PV, Mathaudhu S, Powell CA, Devaraj A (2020) Extreme shear-deformation-induced modification of defect structures and hierarchical microstructure in an Al-Si alloy. *Commun Mater* 1:1–7. <https://doi.org/10.1038/s43246-020-00087-x>
- [39] Jiang D, Yu J (2019) Simultaneous refinement and modification of the eutectic Si in hypoeutectic Al-Si alloys achieved via the addition of SiC nanoparticles. *J Mater Res Technol* 8:2930–2943. <https://doi.org/10.1016/j.jmrt.2019.05.001>
- [40] Liu CH, Chen JH, Li C, Wu CL, Li DZ, Li YY (2011) Multiple silicon nanotwins formed on the eutectic silicon particles in Al-Si alloys. *Scr Mater* 64:339–342. <https://doi.org/10.1016/j.scriptamat.2010.10.030>
- [41] Crump J, Qiao XG, Starink MJ (2012) The effect of high-pressure torsion on the behaviour of intermetallic particles present in Al-1Mg and Al-3Mg. *J Mater Sci* 47:1751–1757. <https://doi.org/10.1007/s10853-011-5955-0>
- [42] Ahn SS, Pathan S, Koo JM, Baeg CH, Jeong CU, Son HT, Kim YH, Lee KH, Hong SJ (2018) Enhancement of the mechanical properties in Al-Si-Cu-Fe-Mg alloys with various processing parameters. *Materials (Basel)* 11:2150. <https://doi.org/10.3390/ma11112150>
- [43] Zhilyaev AP, García-Infanta JM, Carreño F, Langdon TG, Ruano OA (2007) Particle and grain growth in an Al-Si alloy during high-pressure torsion. *Scr Mater* 57:763–765. <https://doi.org/10.1016/j.scriptamat.2007.06.029>
- [44] Jiang J-H, Ma A-B, Lu F-M, Saito N, Watazu A, Song D, Zhang P, Nishida Y (2011) Improving corrosion resistance of Al-11mass%Si alloy through a large number of ECAP passes. *Mater Corros* 62:848–852. <https://doi.org/10.1002/maco.200905521>
- [45] El Aal MIA, Kim HS (2014) Wear properties of high pressure torsion processed ultrafine grained Al-7%Si alloy. *Mater Des* 53:373–382. <https://doi.org/10.1016/j.matdes.2013.07.045>
- [46] Vrátná J, Janeček M, Čížek J, Lee DJ, Yoon EY, Kim HS (2013) Mechanical properties and microstructure evolution in ultrafine-grained AZ31 alloy processed by severe plastic deformation. *J Mater Sci* 48:4705–4712. <https://doi.org/10.1007/s10853-013-7151-x>
- [47] Gubicza J (2019) Lattice defects and their influence on the mechanical properties of bulk materials processed by severe plastic deformation. *Mater Trans* 60:1230–1242. <https://doi.org/10.2320/matertrans.MF201909>
- [48] Zhao YH, Liao XZ, Zhu YT, Horita Z, Langdon TG (2005) Influence of stacking fault energy on nanostructure formation under high pressure torsion. *Mater Sci Eng A* 410–411:188–193. <https://doi.org/10.1016/j.msea.2005.08.074>
- [49] Edalati K, Akama D, Nishio A, Lee S, Yonenaga Y, Cubero-Sesin JM, Horita Z (2014) Influence of dislocation-solute atom interactions and stacking fault energy on grain size of

- single-phase alloys after severe plastic deformation using high-pressure torsion. *Acta Mater* 69:68–77. <https://doi.org/10.1016/j.actamat.2014.01.036>
- [50] Shen, YF, Guan RG, Zhao ZY, Misra RDK (2015) Ultrafine-grained Al-0.2Sc-0.1Zr alloy: The mechanistic contribution of nano-sized precipitates on grain refinement during the novel process of accumulative continuous extrusion. *Acta Mater* 100:247–255. <https://doi.org/10.1016/j.actamat.2015.08.043>.
- [51] Ungár T (2004) Microstructural parameters from X-ray diffraction peak broadening. *Scr Mater* 51:777–781. <https://doi.org/10.1016/j.scriptamat.2004.05.007>
- [52] Ungár T, Alexandrov I, Zehetbauer M (2000) Ultrafine-grained microstructures evolving during severe plastic deformation. *Jom* 52:34–36. <https://doi.org/10.1007/s11837-000-0129-6>
- [53] Kilmametov A, Kulagin R, Mazilkin A, Seils S, Boll T, Heilmaier M, Hahn H (2019) High-pressure torsion driven mechanical alloying of CoCrFeMnNi high entropy alloy. *Scr Mater* 158:29–33. <https://doi.org/10.1016/j.scriptamat.2018.08.031>
- [54] Rajender G, Giri PK (2016) Strain induced phase formation, microstructural evolution and bandgap narrowing in strained TiO<sub>2</sub> nanocrystals grown by ball milling. *J Alloys Compd* 676:591–600. <https://doi.org/10.1016/j.jallcom.2016.03.154>
- [55] Tóth LS, Estrin Y, Lapovok R, Gu C (2010) A model of grain fragmentation based on lattice curvature. *Acta Mater* 58:1782–1794. <https://doi.org/10.1016/j.actamat.2009.11.020>
- [56] Yu PF, Cheng H, Zhang LJ, Zhang H, Jing Q, Ma MZ, Liaw PK, Li G, Liu RP (2016) Effects of high pressure torsion on microstructures and properties of an Al<sub>0.1</sub>CoCrFeNi high-entropy alloy. *Mater Sci Eng A* 655:283–291. <https://doi.org/10.1016/j.msea.2015.12.085>.
- [57] Wang X, Nie M, Wang CT, Wang SC, Gao N (2015) Microhardness and corrosion properties of hypoeutectic Al-7Si alloy processed by high-pressure torsion. *Mater Des* 83:193–202. <https://doi.org/10.1016/j.matdes.2015.06.018>
- [58] Rane GK, Welzel U, Meka SR, Mittemeijer EJ (2013) Non-monotonic lattice parameter variation with crystallite size in nanocrystalline solids. *Acta Mater* 61:4524–4533. <https://doi.org/10.1016/j.actamat.2013.04.021>
- [59] Pippin R (2009) High-Pressure Torsion - Features and Applications. *Bulk Nanostructured Mater*, pp 217–233. <https://doi.org/10.1002/9783527626892.ch9>.
- [60] Qi Y, Kosinova A, Kilmametov AR, Straumal BB, Rabkin E (2018) Generation and healing of porosity in high purity copper by high-pressure torsion. *Mater Charact* 145:1–9. <https://doi.org/10.1016/j.matchar.2018.08.023>
- [61] Wegner M, Leuthold J, Peterlechner M, Setman D, Zehetbauer M, Pippin R, Sergiy V (2013) Percolating porosity in ultrafine grained copper processed by High Pressure Torsion by High Pressure Torsion. *J Appl Phys*, 183509. <https://doi.org/10.1063/1.4829705>.
- [62] Prangnell PB, Bowen JR, Apps PJ (2004) Ultra-fine grain structures in aluminium alloys by severe deformation processing. *Mater Sci Eng A* 375–377:178–185. <https://doi.org/10.1016/j.msea.2003.10.170>
- [63] Cepeda-Jiménez CM, García-Infanta JM, Zhilyaev AP, Ruano OA, Carreño F (2011) Influence of the thermal treatment on the deformation-induced precipitation of a hypoeutectic Al-7 wt% Si casting alloy deformed by high-pressure torsion. *J Alloys Compd* 509:636–643. <https://doi.org/10.1016/j.jallcom.2010.09.122>
- [64] Setman D, Schafler E, Korznikova E, Zehetbauer MJ (2008) The presence and nature of vacancy type defects in nanometals obtained by severe plastic deformation. *Mater Sci Eng A* 493:116–122. <https://doi.org/10.1016/j.msea.2007.06.093>
- [65] Slotwinski JA, Garboczi EJ, Hebenstreit KM (2014) Porosity measurements and analysis for metal additive manufacturing process control. *J Res Natl Inst Stand Technol* 119:494–528. <https://doi.org/10.6028/jres.119.019>
- [66] Lu XJ, Xiao P (2007) Constrained sintering of YSZ/Al<sub>2</sub>O<sub>3</sub> composite coatings on metal substrates produced from electrophoretic deposition. *J Eur Ceram Soc* 27:2613–2621. <https://doi.org/10.1016/j.jeurceramsoc.2006.09.016>
- [67] Bai S, Perevoshchikova N, Sha Y, Wu X (2019) The effects of selective laser melting process parameters on relative density of the AlSi10Mg parts and suitable procedures of the archimedes method. *Appl Sci* 9. <https://doi.org/10.3390/app9030583>.
- [68] Hohenwarter A, Bachmaier A, Gludovatz B, Scherlauer S, Pippin R (2009) Technical parameters affecting grain refinement by high pressure torsion. *Int J Mater Res* 100:1653–1661. <https://doi.org/10.3139/146.110224>
- [69] Valiev RZ, Islamgaliev RK, Alexandrov IV (2000). Bulk nanostructured materials from severe plastic deformation. *Progress Mater Sci*. [https://doi.org/10.1016/S0079-6425\(99\)00007-9](https://doi.org/10.1016/S0079-6425(99)00007-9)
- [70] Furukawa M, Horita Z, Nemoto M, Valiev RZ, Langdon TG (1996) Microhardness measurements and the hall-petch relationship in an Al-Mg alloy with submicrometer grain size. *Acta Mater* 44:4619–4629. [https://doi.org/10.1016/1359-6454\(96\)00105-X](https://doi.org/10.1016/1359-6454(96)00105-X)
- [71] Bazarnik P, Huang Y, Lewandowska M, Langdon TG (2015) Structural impact on the Hall-Petch relationship in an Al-5Mg alloy processed by high-pressure torsion. *Mater Sci*

- Eng A 626:9–15. <https://doi.org/10.1016/j.msea.2014.12.027>
- [72] Furukawa M, Iwahashi Y, Horita Z, Nemoto M, Tsenev NK, Valiev RZ, Langdon TG (1997) Structural evolution and the Hall-Petch relationship in an Al-Mg-Li-Zr alloy with ultra-fine grain size. *Acta Mater* 45:4751–4757. [https://doi.org/10.1016/S1359-6454\(97\)00120-1](https://doi.org/10.1016/S1359-6454(97)00120-1)
- [73] Sato YS, Urata M, Kokawa H, Ikeda K (2003) Hall-Petch relationship in friction stir welds of equal channel angular-pressed aluminium alloys. *Mater Sci Eng A* 354:298–305. [https://doi.org/10.1016/S0921-5093\(03\)00008-X](https://doi.org/10.1016/S0921-5093(03)00008-X)
- [74] Hall EO (1951) The deformation and ageing of mild steel: III Discussion of results. *Proc Phys Soc Sect B* 64:747–753. <https://doi.org/10.1088/0370-1301/64/9/303>
- [75] Petch NJ (1953) The cleavage strength of polycrystals, *Journal of Iron and Steel Institute*. *J Iron Steel Inst* 174:25–28
- [76] Armstrong R, Codd I, Douthwaite RM, Petch NJ (1962) The plastic deformation of polycrystalline aggregates. *Philos Mag* 7:45–58. <https://doi.org/10.1080/14786436208201857>
- [77] Hansen N, Huang X, Hughes DA (2001) Microstructural evolution and hardening parameters. *Mater Sci Eng A* 317:3–11. [https://doi.org/10.1016/S0921-5093\(01\)01191-1](https://doi.org/10.1016/S0921-5093(01)01191-1)
- [78] Gubicza J, Chinh NQ, Csanádi T, Langdon TG, Ungár T (2007) Microstructure and strength of severely deformed fcc metals. *Mater Sci Eng A* 462:86–90. <https://doi.org/10.1016/j.msea.2006.02.455>
- [79] Balogh L, Ungár T, Zhao Y, Zhu YT, Horita Z, Xu C, Langdon TG (2008) Influence of stacking-fault energy on microstructural characteristics of ultrafine-grain copper and copper-zinc alloys. *Acta Mater* 56:809–820. <https://doi.org/10.1016/j.actamat.2007.10.053>
- [80] Wang G, Ouyang H, Fan C, Guo Q, Li Z, Yan W, Li Z (2020) The origin of high-density dislocations in additively manufactured metals. *Mater Res Lett* 8:283–290. <https://doi.org/10.1080/21663831.2020.1751739>
- [81] Zhang XX, Knoop D, Andrä H, Harjo S, Kawasaki T, Lutz A, Lahres M (2021) Multiscale constitutive modeling of additively manufactured Al–Si–Mg alloys based on measured phase stresses and dislocation density. *Int J Plast* 140:102972. <https://doi.org/10.1016/j.ijplas.2021.102972>
- [82] Gubicza J, Dobatkin SV, Khosravi E, Kuznetsov AA, Lábár JL (2011) Microstructural stability of Cu processed by different routes of severe plastic deformation. *Mater Sci Eng A* 528:1828–1832. <https://doi.org/10.1016/j.msea.2010.11.026>
- [83] Wu J, Wang XQ, Wang W, Attallah MM, Loretto MH (2016) Microstructure and strength of selectively laser melted AlSi10Mg. *Acta Mater* 117:311–320. <https://doi.org/10.1016/j.actamat.2016.07.012>
- [84] Zhang JS (2010) High temperature deformation and fracture of materials. Woodhead Publishing. <https://doi.org/10.1533/9780857090805>
- [85] Gao Q, Zhang H, Yang R, Fan Z, Liu Y, Wang J, Geng X, Gao Y, Shang S, Du Y, Liu Z (2018) Effect of alloying elements on the stacking fault energies of dilute Al-based alloys. *J Min Metall Sect B Metall* 54:185–196. <https://doi.org/10.2298/JMMB180107007G>
- [86] Muzyk M, Pakiela Z, Kurzydłowski KJ (2011) Ab initio calculations of the generalized stacking fault energy in aluminium alloys. *Scr Mater* 64:916–918. <https://doi.org/10.1016/j.scriptamat.2011.01.034>
- [87] Muzyk M, Pakiela Z, Kurzydłowski KJ (2018) Generalized stacking fault energies of aluminum alloys-density functional theory calculations. *Metals (Basel)* 8:12–14. <https://doi.org/10.3390/met8100823>
- [88] Geng Y, Wang Y, Xu J, Mi S, Fan S, Xiao Y, Wu Y, Luan J (2021) A high-strength AlSiMg1.4 alloy fabricated by selective laser melting. *J Alloys Compd* 867:159103. <https://doi.org/10.1016/j.jallcom.2021.159103>
- [89] Zamani M, Seifeddine S, Jarfors AEW (2015) High temperature tensile deformation behavior and failure mechanisms of an Al-Si-Cu-Mg cast alloy - The microstructural scale effect. *Mater Des* 86:361–370. <https://doi.org/10.1016/j.matdes.2015.07.084>
- [90] Salas Reyes AE, Altamirano Guerrero G, Rodríguez Ortiz G, Reyes Gasga J, García Robledo JF, Lozada Flores O, Costa PS (2020) Microstructural, microscratch and nanohardness mechanical characterization of secondary commercial HPDC AlSi9Cu3-type alloy. *J Mater Res Technol* 9:266–282. <https://doi.org/10.1016/j.jmrt.2020.05.098>
- [91] Chen Y, Gao N, Sha G, Ringer SP, Starink MJ (2015) Strengthening of an Al-Cu-Mg alloy processed by high-pressure torsion due to clusters, defects and defect-cluster complexes. *Mater Sci Eng A* 627:10–20. <https://doi.org/10.1016/j.msea.2014.12.107>
- [92] Amirjan M, Bozorg M, Sakiani H (2021) Investigation of microstructure and corrosion behavior OF IN718 superalloy fabricated by selective laser melting. *Mater Chem Phys* 263:124368. <https://doi.org/10.1016/j.matchemphys.2021.124368>
- [93] Deaquino-Lara R, Soltani N, Bahrami A, Gutiérrez-Castañeda E, García-Sánchez E, Hernandez-Rodríguez MAL (2015) Tribological characterization of Al7075-graphite composites fabricated by mechanical alloying and hot extrusion. *Mater Des* 67:224–231. <https://doi.org/10.1016/j.matdes.2014.11.045>
- [94] Immanuel RJ, Panigrahi SK (2015) Influence of cryorolling on microstructure and mechanical properties of a cast

- hypoeutectic Al-Si alloy. Mater Sci Eng A 640:424–435. <https://doi.org/10.1016/j.msea.2015.06.019>
- [95] Mungole T, Kumar P, Kawasaki M, Langdon TG (2014) A critical examination of the paradox of strength and ductility in ultrafine-grained metals. J Mater Res 29:2534–2546. <https://doi.org/10.1557/jmr.2014.272>
- [96] Gode C, Yilmazer H, Ozdemir I, Todaka Y (2014) Microstructural refinement and wear property of Al-Si-Cu composite subjected to extrusion and high-pressure torsion. Mater Sci Eng A 618:377–384. <https://doi.org/10.1016/j.msea.2014.09.011>

**Publisher's Note** Springer Nature remains neutral with regard to jurisdictional claims in published maps and institutional affiliations.